Princeton Plasma Physics Laboratory

PPPL- 4750

PPPL- 4750

Layout And Results From The Initial Opeeration Of The High-resolution X-ray Imaging Crystal Spectrometer On The Large Helical Device

N.A. Pablant, M. Bitter, L. Delgado-Apricio, M. Goto, K.W. Hill, S. Lazerson, S. Morita, A.L. Roquemore, D. Gates, D. Monticello, H. Neilson, A. Reiman, M. Reinke, J.E. Rice and H. Yamada

April, 2012

PPPL PRINCETON PLASMA PHYSICS LABORATORY

Prepared for the U.S. Department of Energy under Contract DE-AC02-09CH11466.

Princeton Plasma Physics Laboratory
Report Disclaimers

Full Legal Disclaimer

Trademark Disclaimer

PPPL Report Availability

Princeton Plasma Physics Laboratory:

http://www.pppl.gov/techreports.cfm

Office of Scientific and Technical Information (OSTI):

http://www.osti.gov/bridge

Related Links:

U.S. Department of Energy

Office of Scientific and Technical Information

Fusion Links

Layout and results from the initial operation of the high-resolution x-ray imaging crystal spectrometer on the Large Helical Device

N.A. Pablant,[1] M. Bitter,[1] L. Delgado-Aparicio,[1] M. Goto,[2] K.W. Hill,[1] S. Lazerson,[1] S. Morita,[2] A.L. Roquemore,[1] D. Gates,[1] D. Monticello,[1] H. Nielson,[1] A. Reiman,[1] M. Reinke,[3] J.E. Rice,[3] and H. Yamada[2]

[1)] *Princeton Plasma Physics Laboratory, Princeton, New Jersey 08543, USA*

[2)] *National Institute for Fusion Science, Toki 509-5292, Gifu, Japan*

[3)] *Plasma Science Fusion Center, MIT, Cambridge, Massachusetts 02139-4307, USA*

(Dated: 3 April 2012)

First results of ion and electron temperature profile measurements from the x-ray imaging crystal spectrometer (XICS) diagnostic on the Large Helical Device (LHD) are presented. This diagnostic system has been operational since the beginning of the 2011 LHD experimental campaign and is the first application of the XICS diagnostic technique to helical plasma geometry. The XICS diagnostic provides measurements of ion and electron temperature profiles in LHD with a spatial resolution of 2cm and a time resolution of $\geq$ 10ms. Ion temperature profiles from the XICS diagnostic are possible under conditions where charge exchange recombination spectroscopy (CXRS) is not possible (high density) or is perturbative to the plasma (low density or radio frequency heated plasmas). Measurements are made by using a spherically bent crystal to provide a spectrally resolved 1D image of the plasma from line integrated emission of helium-like Ar^{16+}. The final hardware design and configuration are detailed along with the calibration procedures. Line-integrated ion and electron temperature measurements are presented, and the measurement accuracy is discussed. Finally central temperature measurements from the XICS system are compared to measurements from the Thomson scattering and CXRS systems, showing excellent agreement.

I. INTRODUCTION

A high-resolution x-ray imaging crystal spectrometer (XICS) has recently been installed on the Large Helical Device (LHD) for measurements of the ion and electron temperature profiles and profiles of the poloidal plasma flow velocity with a spatial resolution of ∼2cm and a time resolution of ≥ 10ms. The installation and alignment was completed in May 2011 and the diagnostic has been routinely taking data since the beginning of the 2011 experimental campaign in July.

Measurements of ion and electron temperature profiles are crucial for the investigation of helical plasmas. These measurements are particularly important for the understanding of plasma heating and heat transport within the plasma. While direct measurement of the temperature of the main ion species (hydrogen or deuterium) is difficult, measurements of impurity species can, in many cases, be used as a proxy measurement as long as the ion-ion thermal equilibrium time is sufficiently short. In current tokamak and stellarator devices, including LHD, measurements of the impurity ion temperature are most commonly made using diagnostics based on charge exchange recombination spectroscopy (CXRS). The recent invention and development of the x-ray imaging crystal spectrometer Ref. 1,2 and advances in x-ray detector technology Ref. 3 have made it possible to obtain profiles of the ion temperature, electron temperature and plasma flow velocity, with high spatial and temporal resolutions, from analysis of x-ray spectra from highly ionized impurities in the plasma. XICS is now used as a primary ion temperature diagnostic on several existing fusion devices, including Alcator C-Mod, EAST and KSTAR, and is planned to be the primary core ion temperature diagnostic for ITER.

In LHD, XICS provides ion temperature profiles in both high and low density plasma conditions where measurements from CXRS are not available or difficult to make. At high densities, the neutral beams cannot penetrate to the core, and CXRS is available only in the plasma edge. At low densities, the use of the perpendicular neutral beam injection (NBI) results in a plasma density increase, and can significantly perturb the plasma. In addition, because XICS does not rely on neutral beam injection, it is an ideal diagnostic for the investigation of radio frequency heated plasmas, especially in steady state scenarios, and for studying the dynamics of neutral beam heating. By providing measurements in this wider range of plasma conditions, the XICS diagnostic is expected to become an integral

part of the LHD physics program.

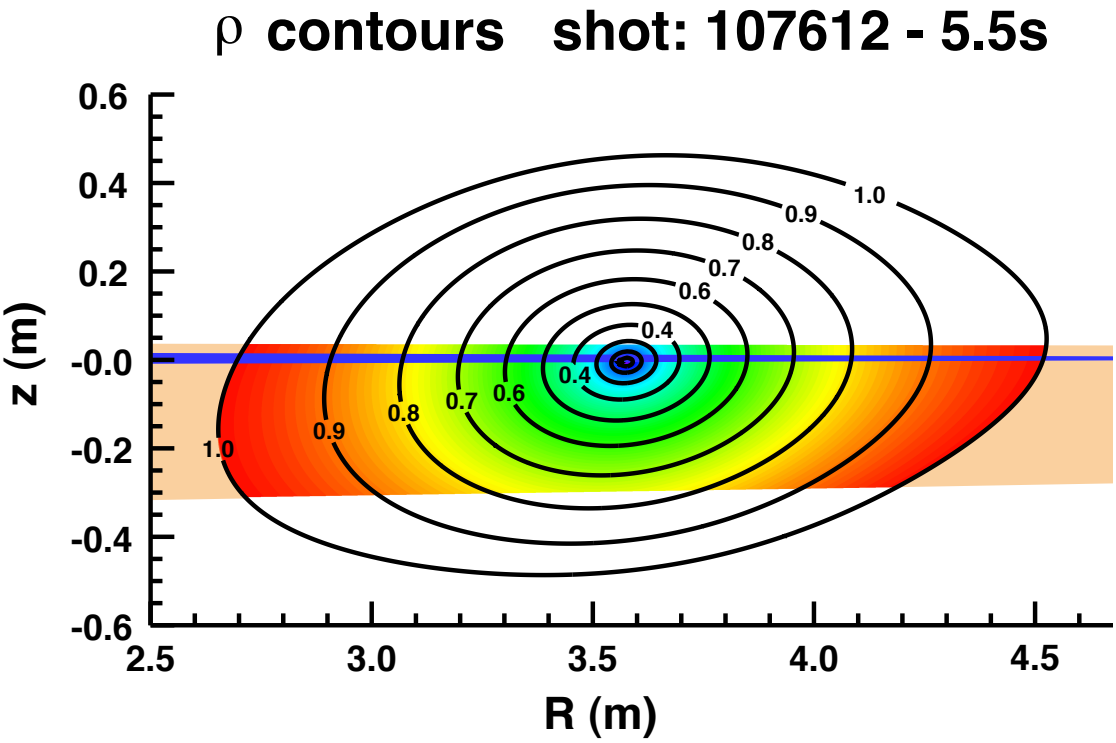

FIG. 1. Contour plot of flux surfaces for shot 107612 showing the spatial range covered by the XICS sightlines. The viewing range corresponding to a single pixel on the detector is shown in blue. Flux surfaces are determined by a STELLOPT equilibrium reconstruction. The flux surface contours are found by tracing the XICS sightlines through the VMEC equilibrium solution in 3D. What is shown is not a planar cut, but rather a map of the true sightline geometry in R and z.

The XICS system on LHD is unique in that it is the first application of this diagnostic to a helical plasma configuration. This implementation is extremely important as it has accelerated the development of 3D equilibrium reconstruction tools which are necessary for interpretation of the line-integrated XICS measurements. Additionally this installation will allow, for the first time, a thorough comparison of the XICS diagnostic with the more broadly tested CXRS and Thomson scattering systems. A discussion on the consequences of the heliotron geometry and the original design goals for the LHD XICS diagnostic system have been presented previously by Bitter *et al.*[4] and Pablant *et al.*[5]. In this paper the final hardware layout and viewing geometry of the LHD XICS diagnostic will be documented and the spatial calibration procedures described. Ion and electron temperature measurements from the system will be presented, showing the typical performance characteristics of the diagnostic. Finally the XICS measurement will be compared against existing diagnostics,

demonstrating excellent agreement.

The XICS system was designed to have full coverage of the plasma cross-section, and to measure poloidal plasma rotation in addition to the ion and electron temperature. However, for the initial installation, described in this paper, a smaller detector was used, providing only a third of designed spatial coverage (see Fig.1). With this limited spatial coverage it is difficult to verify and interpret measurements of the plasma flow, therefore these measurements will not be discussed in the present paper. In addition, to provide adequate time for cooling, the presently used detector is limited to operation on every other shot and provides a maximum data window of 15s. An upgrade for the 2012 experimental campaign will allow the diagnostic to operate at its design parameters.

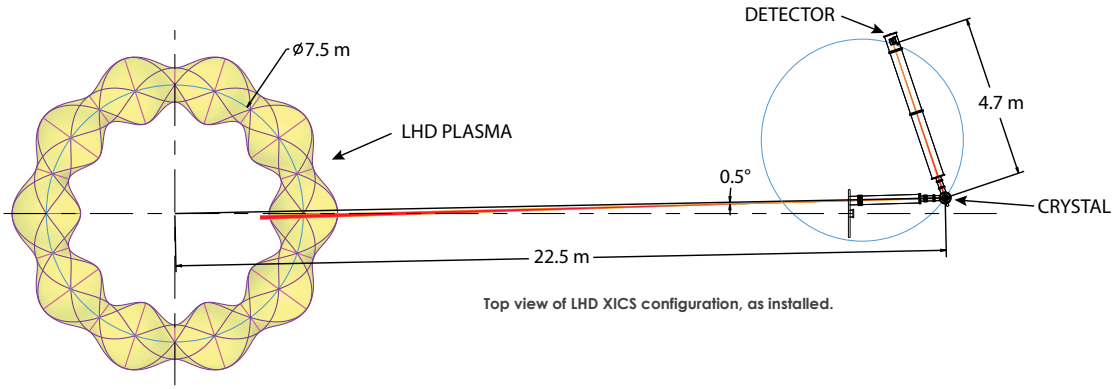

FIG. 2. Top down view of the XICS layout.

II. DIAGNOSTIC TECHNIQUE

The XICS diagnostic utilizes a spherically bent quartz crystal to provide a 1D image of line integrated spectra from highly charged impurity species in the plasma. The diagnostic concept has been explained in detail by Bitter *et al.*[4] and Ince-Cushman *et al.*[6]; a conceptual diagram of the diagnostic layout can be found in figure 2 of Ref. 4. The XICS system on LHD has been designed to view impurity emission from helium-like Ar^{16+} which is the predominant argon ionization state for typical LHD core electron temperatures in the range of 1 to 3keV (see Ref. 7 §2.3). Argon injection is typically non-perturbative to the plasma,

is regularly introduced into LHD for diagnostic purposes, and has well understood x-ray spectra.

Because of the lack of toroidal symmetry, as well as the available installation locations, a modification to the diagnostic design typically used on tokamak systems was required. In particular, the system is designed with a smaller spectral extent, but with a higher spectral resolution. With this configuration the toroidal extent of the views in the plasma due to the astigmatism in the XICS optics layout is matched to the toroidal spread due to the variation in Bragg angle across the spectral range. The final configuration provides spectral coverage from 3.941 to 3.962$\mathring{A}$. With this spectral range only the resonance line ($1s2p\ (^1P_1) \rightarrow 1s^2\ (^1S_0)$), also known as the w line, and the $n \geq 3$ satellites ($1s2lnl' \rightarrow 1s^2nl''$)are visible on the detector.

Measurements of the ion-temperature (T_i) are made from the Doppler broadening of the spectral lines, while the electron temperature (T_e) is found from the relative intensities of $n \geq 3$ dielectronic satellite lines to the resonant emission line. In addition to temperature measurements, the XICS system can also be used to measure the plasma flow velocity from the Doppler shifts of the spectral lines and measure the density of Ar^{16+} from the intensity of resonance line.

Measurements of the plasma flow require that the Doppler shifts of the lines are measured with very high accuracy, especially on LHD where plasma flows are expected to be ≈5km/s. For the LHD XICS system a measurement of the poloidal rotation with 1km/s accuracy requires that the lines shifts are measured to within 0.01$m\mathring{A}$, which corresponds to 0.1pixels on the detector. Preliminary measurements of line shifts with this accuracy exceeding 0.1pixels have been made, however because the diagnostic only sees the overlapping resonance and $n \geq 3$ satellite lines, any inaccuracies in the location, relative intensities, or shape of the lines in the atomic physics model can potentially cause changes in the electron temperature to produce an apparent line shift in the spectral fit. To verify the accuracy of a poloidal flow measurement it is important to compare results made from viewing the upper and lower half of the plasma cross-section, which will produce Doppler shifts in opposite directions; however, this comparison is not possible with the current initial limited installation, where only a third of the plasma can be viewed. Poloidal flow measurements are expected to be available in 2012 after an upgrade of the system that will provide full plasma coverage of the plasma cross-section.

To determine the line intensities, locations and widths, an atomic physics based spectral model is fitted to the recorded line-integrated spectra. For this spectral fitting, atomic data from the MZ code is used for the line locations and for the relative intensities of the satellite lines[8]. Each spectral line is modeled as a Voigt profile, taking into account the Doppler broadening and natural line width. The effect of instrumental line broadening on the ion temperature measurements is expected to be less than 10eV and is neglected. A spectrum fitted using this model is shown in Fig.4. The electron temperature is calculated from the fitted line intensities using excitation rate coefficients calculated with the AUTOSTRUCTURE code[9,10]. Details of the spectral model and the spectral fitting process will be discussed in a forthcoming publication.

In order to find local values for T_i and T_e from the line integrated spectrum, an inversion of the data is required. This inversion is possible with a reconstruction of the plasma equilibrium and the following assumptions: that the plasma emissivity and temperature are constant on flux surfaces and that the ion energy distribution is Maxwellian. Plasma reconstructions are done using a set of reconstruction codes, VMEC, STELLOPT and PIES, being developed for LHD at PPPL[11].

When the Ar^{16+} emissivity is highly peaked, the line integrated measurements will provide a good approximation to the local plasma parameters at the flux surface tangency location. As the emissivity profile becomes flat or hollow, the line integrated measurements no longer provide a good local approximation, and inversion techniques are necessary. In this paper only line-integrated results will be presented. Inverted profile measurements from the XICS diagnostic utilizing reconstructions from STELLOPT will be presented in a future paper.

III. HARDWARE LAYOUT

The crystal installed in the present system is a 70μm thick 110-quartz crystal with a 2d-spacing of 4.91352$\mathring{A}$[12]. The crystal dimensions are 4cm in the horizontal (spectral) direction and 10cm in the vertical (spatial) direction. These dimensions were chosen to maximize throughput while retaining a spatial resolution of 2cm vertically in the plasma and a toroidal viewing extent of 10cm which matches the spectral range and the scale length of the helical magnetic field.[4] The crystal is placed onto a 13cm spherical substrate and held in place through electrostatic forces. The radius of curvature of the crystal has been measured to be

Crystal			
location	22.47380 (x)	0.45500 (y)	0.00000 (z)
normal	−0.82073	0.57132	0.00117
$\hat{x}'$	−0.57132	−0.82073	0.00000

Detector			
location	20.95609 (x)	4.94127 (y)	0.04170 (z)
normal	0.31950	−0.94759	−0.00155
$\hat{x}'$	−0.94759	−0.31950	0.00073

TABLE I. Location and orientation of crystal and detector given in machine coordinates, (x, y, z). To specify the orientation of the detector and crystal we define a local coordinate system (x', y', z') where z' is along the normal to the surface at the center of the detector/crystal. The orientation of the crystal and detector can now be described in machine coordinates using the normal and $\hat{x}'$ unit vectors. Machine coordinates are defined so that the x axis is aligned with the 7–0 port. Location values are in meters.

5896±2mm. In order to allow the system to be aligned optically, a 130$\mathring{A}$ thick aluminum coating was placed over the front surface of the crystal and substrate.

In order to avoid attenuation of the x-ray signal in air, the system is operated under vacuum. The crystal chamber is separated from the LHD vacuum vessel by a 6inch diameter beryllium window of thickness 0.004inch, supported by a 0.020inch thick beryllium honeycomb structure on either side. This window provides protection to LHD and allows the diagnostic to be operated at a higher vacuum pressure (10Pa) than the main LHD vessel.

The final calibrated values for the crystal and detector positions are given in Table I. The crystal is placed at a distance of 22.48m from the center of LHD, and oriented so that the resonance line sightlines have an angle of 0.5° from the radial direction at the crystal surface, see Fig.2. The detector is placed on the Rowland circle for the resonance line at a distance of 4.74m from the crystal and oriented to be perpendicular to the ray of the resonance line that is reflected from the center of the crystal.

In the configuration used for the 2011 experimental campaign a single Pilatus 100K-S detector system is used. The Pilatus detector was developed by the Paul Scherrer Institute and is commercially produced by Dectris.[3,13] This detector consists of 195×487pixels with a pixel pitch of $172 \times 172 \mu\text{m}^2$. In the LHD system the detector is arranged so that the spectra are recorded in the short direction and imaging is done in the long dimension.

The Pilatus 100K-S detector was not designed to be operated in a vacuum environment and cannot be actively cooled in the current installation. Temperature control is only

possible via radiative cooling, limiting the continuous time that the detector can be powered on. The shot repetition rate on LHD is 3 minutes. To maintain the detector temperature within the operating range, the detector is only run on even numbered shots and is limited to taking data for a period of 15s. This duration is sufficient to cover the full plasma evolution on the majority of LHD plasma discharges, but does not allow the system to be run continuously during long pulse operation.

The final diagnostic configuration, as described in Table I, provides the a view of the plasma from $z = -0.297$m to $z = 0.037$m, where z is defined where the sightline crosses a major radius of 3.65m. This view results in coverage out to a normalized radius (ρ) of approximately 0.75 (see Fig.1). For mapping of the pixels on the detector to wavelength, the Bragg condition is used along with the final calibrated locations and orientations of the crystal and detector. The final dispersion of the system on the central row of the detector at the resonance line ($3.9492\mathring{A}$[8]) is $0.61723m\mathring{A}$/mm.

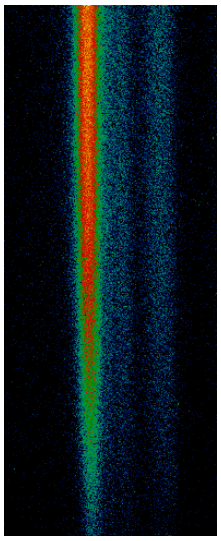

FIG. 3. Raw data from a single timeslice, 20ms integration time. shot 107612 at 6700ms. The bright line on the left hand side is the resonance line, the weaker contributions on the right hand side are from the $n = 3$ dielectronic satellite lines.

IV. SPATIAL CALIBRATION

Precise measurements of the final hardware configuration are critical for the XICS diagnostic to produce accurate ion temperature and plasma rotation measurements. Mapping of the pixels on the detector to wavelength, as required for spectral fitting, requires that the

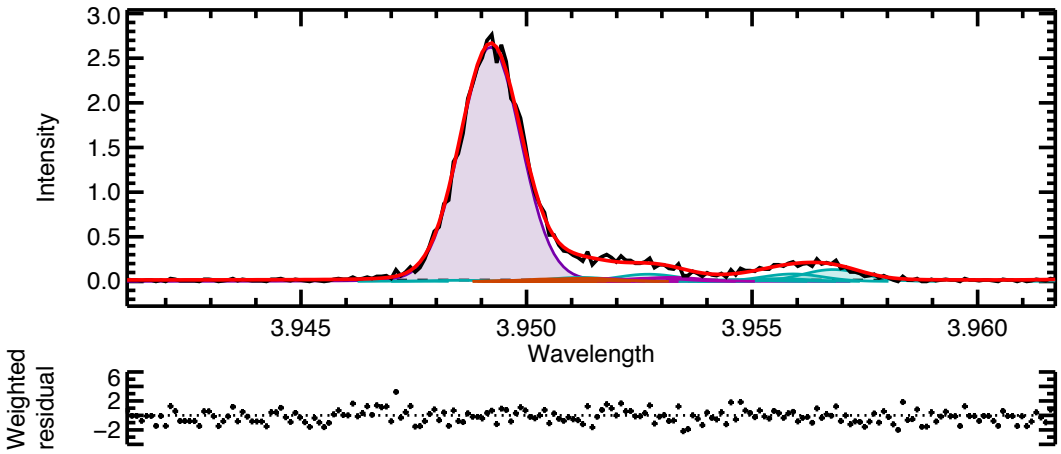

FIG. 4. Spectral fit of a line-integrated Ar^{16+} spectrum recorded by central channels of the XICS system. Raw data are shown in black, the fit to the spectrum is shown in red. The individual lines that make up the final fitted spectrum are superimposed. The weighted residual is defined by $residual = (spectrum - fit)/\sigma_{spectrum}$. Shot 107612, 60ms integration time, 44 rows are binned providing a spectral resolution of ≈4cm.

relative distance and orientation between the crystal and the detector are known. Moreover, to obtain temperature and rotation profiles, inferred from an inversion of the line-integrated measurements, requires knowledge of the sightline geometry, for which the location and orientation of the crystal with respect to the plasma must be precisely measured.

The configuration accuracy needed for sightline determination and ion temperature measurements are fairly modest, requiring that the crystal and detector locations are know to within several millimeters. Measurements of the plasma rotation however require a much more precise characterization of the system configuration, with the detector location calibrated to within 20μm and 0.03°, which corresponds to a wavelength accuracy of $0.01m\mathring{A}$. An alignment and calibration procedure, described in this section, has been developed that can meet these requirements, and which is also generally applicable to XICS diagnostics installed on other devices.

To obtain plasma flow measurements with 1km/s accuracy, the Doppler shift of the spectral lines must be measured with an accuracy of $10^{-5}\mathring{A}$. This accuracy is higher than the uncertainty in the theoretical or experimental unshifted Ar^{16+} line wavelengths of approximately $10^{-4}\mathring{A}$.[8,14] Because of the uncertainty in the helium-like Argon line wavelengths, and given that an absolute wavelength reference is currently unavailable, a relative calibra-

tion is completed through the use of a stationary plasma. The calibration described here finds a spatial configuration that is consistent with both the measurements of the diagnostic layout and the best known values for the line wavelengths, and compensates for shifts in the recorded spectra due to the crystal diffraction profile (rocking curve) and spherical aberration of the optics[15].

The alignment and calibration procedure is done in several steps. First an alignment procedure is completed that provides the location and orientation of the detector and crystal with an accuracy of several millimeters. Finally a calibration procedure, based on emission from a non-rotating plasma, allows the detector location, relative to the crystal, to be determined with our desired accuracy of better than 20μm.

Careful alignment of the crystal and detector were completed using a combination of laser alignment and triangulation. First the crystal and detector chambers are placed at the desired locations with respect to the LHD vacuum vessel. This careful placement ensures that the angle between the center of the two diagnostic arms is matched to the Bragg angle for the He-like argon resonance line. Auto-alignment of the crystal is then completed by using a self-leveling laser placed at the end of the crystal-detector arm and configured so as to be coincident with the center of the diagnostic vacuum chamber. The crystal orientation is then adjusted so that the laser beam, which falls on the center of the crystal, is reflected back to its source. The crystal is finally turned about a separately adjustable vertical axis until the laser passes through the center of the crystal-LHD arm and onto center scribe marks placed on the gate valves.

After alignment of the crystal and detector mount, an in-vessel calibration is performed to provide measurements on the final diagnostic configuration and allow the final viewing volume within the plasma to be recorded. The in-vessel calibration is done by removing the detector and illuminating the crystal with a visible light point source placed at the detector location. The point light source is created by focusing a 2.0mW low divergence He-Ne laser through a 50mm focal length lens. For this calibration a mask is added in front of the crystal substrate so that only the rectangular crystal surface is illuminated. Planar targets are set up at several locations in the LHD vacuum vessel, referenced to fixed points, and the illumination pattern is recorded. An image of the target with the laser illumination pattern can be found in Figure 4 of Ref. 5.

The procedure described above provides an alignment of the detector and crystal with

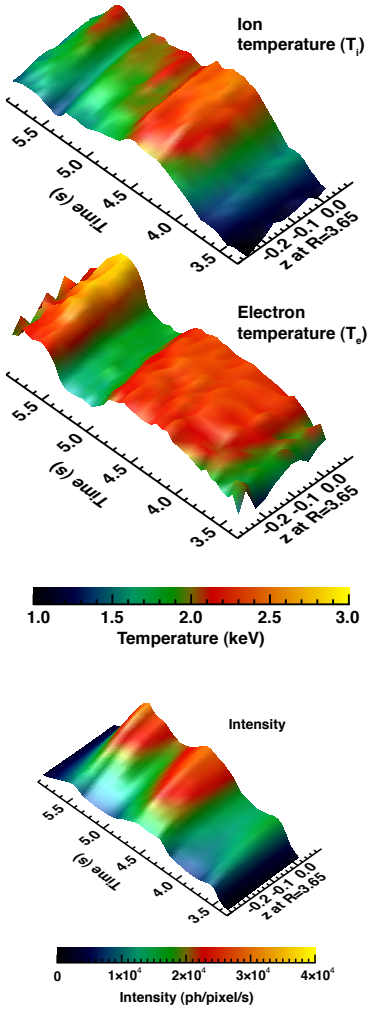

FIG. 5. Surface plots of, T_i, T_e and the intensity of the Ar^{16+} resonance line as measured by the XICS diagnostic. Shot 108642, 60ms time resolution, 4cm spatial resolution (44 rows binned per channel).

an accuracy of 5mm. The next step is to use a calibration procedure to more accurately determine the final detector location. This is done by utilizing recorded spectra taken during a plasma shot which is assumed to have no plasma flows. A least-squares fitting procedure has been developed that allows the detector location and orientation (6 degrees of freedom) to be determined by using these recorded spectra and the measured diagnostic layout as constraints.

The fitting procedure is based on determining the detector location so as to minimize the difference between the expected line locations and the actual recorded line locations for a non-rotating plasma while at the same time minimizing the difference between the measured

detector location and the final calibrated position. The expected location of a wavelength on the detector is determined by intersecting the cone that satisfies the Bragg condition with the plane of the detector, producing an ellipse on the detector.

Before fitting of the detector location can be done, the recorded spectra are analyzed to determine the line positions, in pixels, on every row of the detector. This determination is done by using the detector location measured during the alignment process and fitting the spectra using the atomic physics based spectral model. Since the fitting is done while using an un-calibrated detector location, the calculated mapping from to wavelengths is not expected to be correct at this point in the calibration procedure; therefore, on each row we add a linear wavelength shift to the lines returned by the atomic physics model. Using this technique, line locations can be determined with an accuracy better than 0.1pixels.

To construct a residual for a potential detector location, the line locations on each row, as determined above, are mapped from pixel to wavelength and compared to the expected un-shifted line wavelength, weighted by the uncertainty in the theoretical wavelength calculations. Added to this residual is the difference between the potential detector location and the location measured during the alignment, weighted by the measurement error. A Levenberg-Marquardt algorithm can now be employed to vary the potential detector location so as to minimize this residual.

To ensure self-consistency, after a solution is found the process is repeated using the calibrated detector position, and starting at the determination of the line locations in pixels. The final residuals from the least-squares calibration technique provide a way to check the consistency of the solution with the physical measurements and verify the assumption of a non-rotating plasma. If patterns were seen in the final residuals, it would be an indication that there was an inconsistency in either the assumptions or the measurements.

The results from the calibration procedure described in this section are given in Table I. In this table the location of the detector, relative to the crystal, is determined within 10μm, and the location of the crystal, relative to LHD, is determined within 5mm.

V. PERFORMANCE

The spatial resolution of the system is primarily determined by the crystal size and focusing properties of the system. The viewing volume corresponding to a single pixel leads

to a spatial resolution of ∼2cm, as shown in Fig.1. To match the optical spatial resolution, a minimum of 22 rows on the detector are binned together in software before fitting to form one spatial channel. The viewing volume also has an extent of ∼10cm in the toroidal direction, caused both by the astigmatism of the optical system and by the change in Bragg angle over the wavelength range of the diagnostic. In stellarator geometry, which lacks toroidal symmetry, this extent of the viewing volume in the toroidal direction also limits the achievable spatial resolution.

The time resolution of the system is limited by the readout time of the detector system, which is 2.7ms. During the readout the detector is insensitive, therefore data are typically acquired with a time resolution of 20ms in order to retain a reasonable overall detector live time,.

Line-integrated measurements from the central channels of the XICS diagnostic have been compared with measurements from the Thomson scattering (T_e) and CXRS (T_i) diagnostics. Such a comparison is shown in Fig.6 for shot 108642. Excellent agreement is seen between the diagnostics before 5.5s, when the argon emissivity profile is peaked. As the electron temperature rises after 5.5s the Ar^{16+} in the core burns out, resulting in a hollow emissivity profile. The central XICS chords are now weighted primarily by emission from lower temperature regions away from the core and therefore reflect lower T_e values than the central T_e value measured by Thomson scattering. CXRS measurements are only available when the appropriate neutral beam is on (NBI #4).

Since the three diagnostics have different viewing geometries and are located at different toroidal locations around LHD, profile comparisons can only be done after the measurement from all of the diagnostics have been mapped to flux coordinates. This coordinate mapping requires sightline tracing through an equilibrium reconstruction and will be discussed in a future publication along with inverted results.

The statistical uncertainties in the XICS measurements are dependent on the brightness of the Ar^{16+} emission and therefore on the argon density in the core of LHD. The core argon density is determined both by the amount of argon puffing and by impurity transport, and can vary dramatically from shot to shot. For shots with good argon emissivity the XICS measurement can be made with an accuracy and resolution similar to or exceeding that of Thomson and CXRS.

For the analysis shown in Fig.6 the XICS data are analyzed with 20ms time resolution

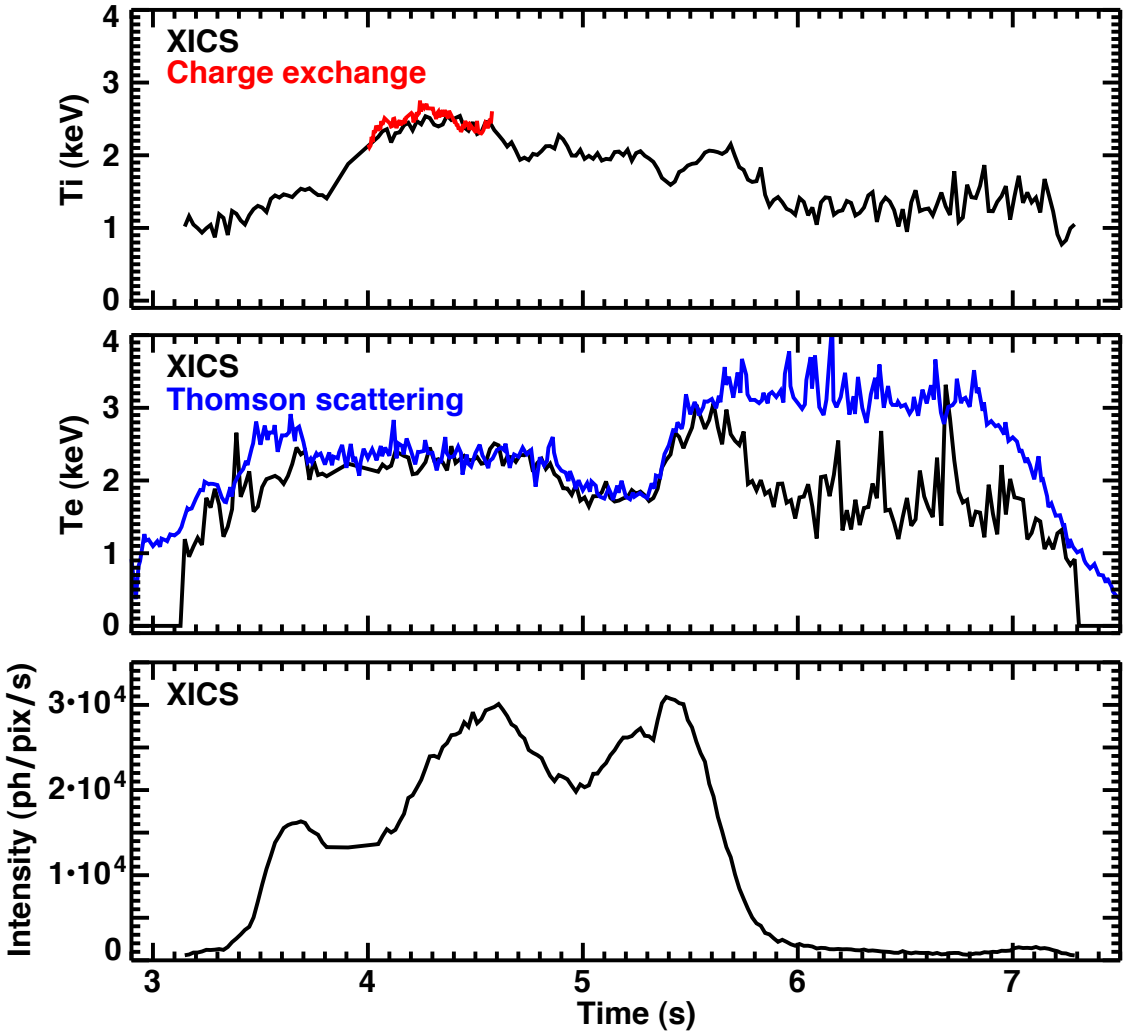

FIG. 6. Central ion and electron temperatures from the XICS diagnostic compared to measurements from the Thomson scattering (T_e) and fast CXRS (T_i) diagnostics. XICS measurements are shown with 20ms time resolution and 2cm spatial resolution (22 rows binned per channel). For the Thomson scattering system 5 central channels have been averaged providing a spatial resolution of 8cm and a time resolution of 6–20ms. For the CXRS system the central channel is shown providing a spatial resolution of ≈5cm and a time resolution of 5ms.

and 2cm spatial resolution for a typical shot with good argon emission intensity of 2.5×10^4photons/pixel/s during the time of interest between 4.0–4.5ms. During this period the uncertainties in temperature measurements are approximately 60eV (3%) and 100eV (5%) for the ion and electron temperatures respectively. These values are taken from the reported uncertainties returned by the non-linear least-squares algorithm (`MPFIT`[16]) and agree with the standard deviation in the time history of the measurements. These uncertainties are comparable to those in the Thomson scattering and CXRS measurements as reported in

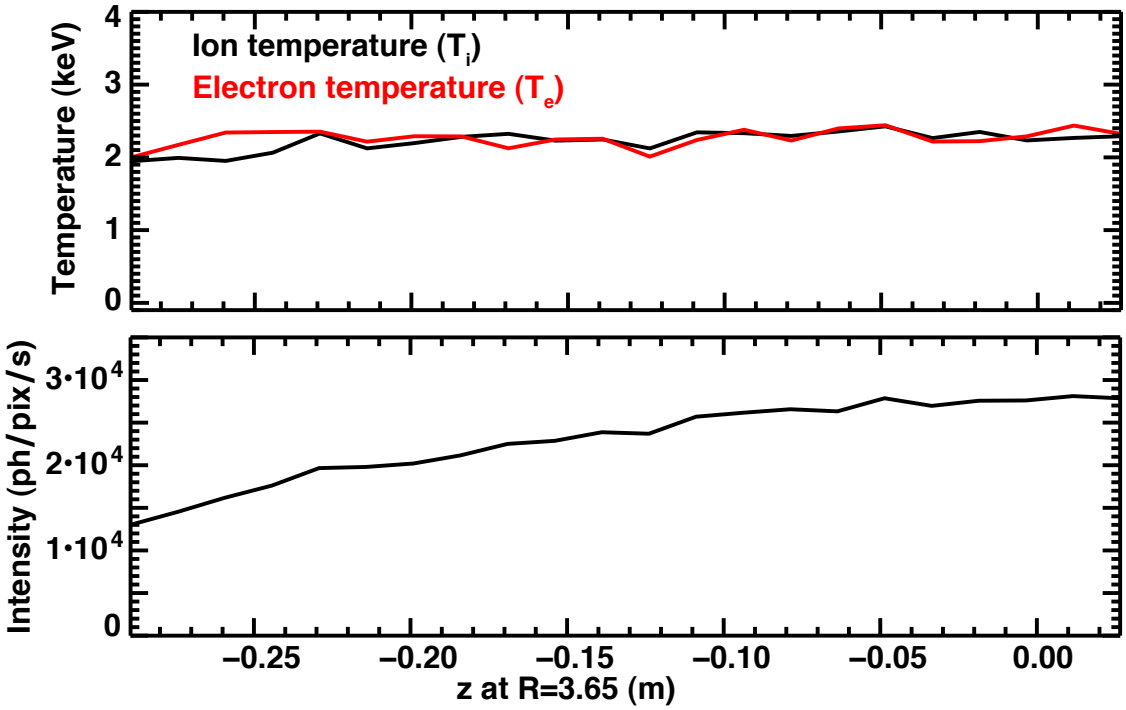

FIG. 7. Profiles of line-integrated measurements from the XICS system. Shot 108642 at 4500ms, 20ms time resolution, 2cm spatial resolution (22 rows binned per channel).

Ref. 17 and Ref. 18.

For ion temperature measurements the relative statistical uncertainty in the final measurements is determined almost entirely by photon statistics; for the electron temperature however, the sensitivity of measurement is better at lower temperatures where a small change in the electron temperature results in a large change in the line intensity ratio.[10] The uncertainty in T_i, σ_{T_i}, is proportional $T_i/\sqrt{I}$, which is obtained by following Ref. 19 while using Poisson statistics for the uncertainly in the recorded spectrum. While a simple analytical expression for the uncertainty in T_e is not available due to the use of numerically calculated rate coefficients, over the temperature range of interest the trend can be well described by $\sigma_{T_i} \propto e^{(E_s-E_0)/T_e} T_e^2/\sqrt{I}$, where E_0 is the energy of the resonance line and E_S is the energy between the $n = 3$ upper satellite level and the He-like ground state. Measurement accuracy can be improved at the expense of resolution by binning of the data in the spatial or temporal directions.

VI. CONCLUSION AND FUTURE PLANS

The first results from the recently installed high resolution x-ray imaging crystal spectrometer on LHD demonstrate that the diagnostic is able to provide profile measurements of the line integrated ion and electron temperature profiles with excellent time (20ms) and spatial resolution (2cm). The current XICS installation provides coverage from of the plasma from $z = -0.297$m to $z = 0.037$m and can be used to measure plasmas with central electron temperatures in the range 0.5–3keV. Central temperatures measured with the XICS system have been compared with measurements made using the Thomson and CXRS diagnostics, and show excellent agreement.

An upgrade of the LHD XICS system is currently underway for the 2012 experimental campaign. As part of this upgrade a larger detector (Pilatus 300K) will be installed which will allow the diagnostic to be operated at its design parameters. With this new detector the entire plasma will be imaged, allowing more accurate inversion of the line integrated spectra. In addition this detector will be water cooled, allowing the diagnostic to take measurements during every shot as well as during long pulse operations. A second crystal will also be added to the system to allow hydrogen-like argon (Ar^{17+}) emission to be simultaneously measured. This addition will allow temperature measurements in plasmas with electron temperatures up to 10keV.

Research supported by the U.S. DOE under Contract No. DE-AC02-09CH11466 with Princeton University.

REFERENCES

[1]M. Bitter, K. W. Hill, B. Stratton, A. L. Roquemore, D. Mastrovito, S. G. Lee, J. G. Bak, M. K. Moon, U. W. Nam, G. Smith, J. E. Rice, P. Beiersdorfer, and B. S. Fraenkel, Review of Scientific Instruments **75**, 3660 (2004).

[2]K. W. Hill, M. L. Bitter, S. D. Scott, A. Ince-Cushman, M. Reinke, J. E. Rice, P. Beiersdorfer, M.-F. Gu, S. G. Lee, C. Broennimann, and E. F. Eikenberry, Review of Scientific Instruments **79**, 10E320 (2008).

[3]C. Broennimann, E. Eikenberry, B. Henrich, R. Horisberger, G. Huelsen, E. Pohl,

B. Schmitt, C. Schulze-Briese, M. Suzuki, T. Tomizaki, *et al.*, J. Synchrotron Rad. **13**, 120 (2006).

[4]M. Bitter, K. Hill, D. Gates, D. Monticello, H. Neilson, A. Reiman, A. L. Roquemore, S. Morita, M. Goto, H. Yamada, and J. E. Rice, Review of Scientific Instruments **81**, 10E328 (2010).

[5]N. A. Pablant, M. Bitter, L. Delgado-Aparicio, M. Goto, K. Hill, S. Lazerson, S. Morita, A. Roquemore, D. Gates, D. Monticello, H. Nielson, A. Reiman, M. Reinke, J. Rice, and H. Yamada, in *Proceedings of the 38th EPS Conference on Plasma Physics* (2011).

[6]A. Ince-Cushman, J. E. Rice, M. Bitter, M. L. Reinke, K. W. Hill, M. F. Gu, E. Eikenberry, C. Broennimann, S. Scott, Y. Podpaly, S. G. Lee, and E. S. Marmar, Review of Scientific Instruments **79**, 10E302 (2008).

[7]A. Ince-Cushman, *Rotation Studies in Fusion Plasmas via Imaging X-ray Crystal Spectroscopy*, Ph.D. thesis, Massachusetts Institute of Technology (2008).

[8]F. Goryayev, A. Urnov, and L. Vainshtein, Arxiv preprint physics/0603164 (2006).

[9]N. R. Badnell, Journal of Physics B: Atomic, Molecular and Optical Physics **30** (1997).

[10]O. Marchuk, *Modeling of He-like spectra measured at the tokamaks TEXTOR and TORE SUPRA*, Ph.D. thesis, Ruhr-Universität Bochum (2004).

[11]S. Lazerson, D. Gates, D. Monticello, H. Neilson, N. Pomphrey, A. Reiman, S. Sakakibara, and Y. Suzuki, in *38th EPS Conference on Plasma Physics* (2011).

[12]W. H. Baur, Z. Kristall. **224**, 580 (2009).

[13]"http://www.dectris.com/sites/pilatus100k.html," (2010).

[14]M. R. Tarbutt, R. Barnsley, N. J. Peacock, and J. D. Silver, Journal of Physics B: Atomic, Molecular and Optical Physics **34**, 3979 (2001).

[15]E. Wang, P. Beiersdorfer, M. Gu, M. Bitter, L. Delgado-Aparicio, K. W. Hill, M. Reinke, J. E. Rice, and Y. Podpaly, Review of Scientific Instruments **81**, 10E329 (2010).

[16]C. B. Markwardt, in *Astronomical Data Analysis Software and Systems XVIII*, Astronomical Society of the Pacific Conference Series, Vol. 411, edited by D. A. Bohlender, D. Durand, & P. Dowler (2009) p. 251, arXiv:0902.2850 [astro-ph.IM].

[17]K. Narihara, I. Yamada, H. Hayashi, and K. Yamauchi, Review of Scientific Instruments **72**, 1122 (2001).

[18]K. Ida, S. Kado, and Y. Liang, Review of Scientific Instruments **71**, 2360 (2000).

[19]H. G. Kaper, D. W. Smits, U. Schwarz, K. Takakubo, and H. van Woerden, Bull. Astr.

Inst. Netherlands **18**, 465 (1966).

The Princeton Plasma Physics Laboratory is operated
by Princeton University under contract
with the U.S. Department of Energy.

Information Services
Princeton Plasma Physics Laboratory
P.O. Box 451
Princeton, NJ 08543

Phone: 609-243-2245
Fax: 609-243-2751
e-mail: pppl_info@pppl.gov
Internet Address: http://www.pppl.gov